coefficients, a topic of considerable current interest in combustion kinetics, for example.

For more complex reactions, involving multiple product channels and/or multiple wells, the competition between channels is strongly dependent on the details of the energy transfer process. It is likely that prior empirical master equation–based calculations for such reactions have largely yielded poor representations of the kinetics, at least for the higher-energy channels. The quantitative prediction of such rate coefficients may require the development of more complete representations of the collision kernel. For example, the competition between two channels with widely disparate rotational constants may require an improved representation of the J' dependence of the kernel, which could perhaps be achieved through quadratic rather than linear expansions of the parameters in eq. S5. Meanwhile, the quantitative modeling of the competition between two channels with quite different thresholds requires an accurate description of the ΔE dependence of the kernel over a broad range of E. Although the stretched exponentials allow some flexibility in this regard, it may also prove necessary to employ a more general representation incorporating, for example, a sum of terms of the form of eq. S3. Such double exponentials have proven useful in studying the effect of high-energy tails (supercollisions) (33) in prior 1DME studies (3, 18, 34). The present single-well single-product case study provides a roadmap for such multiple-product multiple-well analyses.

REFERENCES AND NOTES

1. B. Widom, *Science* **148**, 1555–1560 (1965).
2. K. A. Holbrook, M. J. Pilling, S. H. Robertson, *Unimolecular Reactions* (Wiley, West Sussex, 1996).
3. R. G. Gilbert, S. C. Smith, *Theory of Unimolecular and Recombination Reactions* (Blackwell Scientific, Oxford, UK, 1990).
4. J. A. Miller, S. J. Klippenstein, *J. Phys. Chem. A* **110**, 10528–10544 (2006).
5. D. C. Clary, *Science* **279**, 1879–1882 (1998).
6. D. H. Zhang, M. A. Collins, S.-Y. Lee, *Science* **290**, 961–963 (2000).
7. S. L. Mielke et al., *Phys. Rev. Lett.* **91**, 063201 (2003).
8. T. Wu, H.-J. Werner, U. Manthe, *Science* **306**, 2227–2229 (2004).
9. H. Sabbah et al., *Science* **317**, 102–105 (2007).
10. D. Polino, S. J. Klippenstein, L. B. Harding, Y. Georgievskii, *J. Phys. Chem. A* **117**, 12677–12692 (2013).
11. S. J. Klippenstein, Y. Georgievskii, L. B. Harding, *Phys. Chem. Chem. Phys.* **8**, 1133–1147 (2006).
12. A. W. Jasper, J. A. Miller, S. J. Klippenstein, *J. Phys. Chem. A* **117**, 12243–12255 (2013).
13. V. D. Knyazev, *J. Phys. Chem.* **99**, 14738–14741 (1995).
14. R. Sivaramakrishnan et al., *J. Phys. Chem. A* **115**, 3366–3379 (2011).
15. C. F. Goldsmith, A. S. Tomlin, S. J. Klippenstein, *Proc. Combust. Inst.* **34**, 177–185 (2013).
16. In many works, the total internal energy *E* is replaced with the active energy ε, which represents the vibrational energy of the molecule.
17. S. C. Smith, R. G. Gilbert, *Int. J. Chem. Kinet.* **20**, 307–329 (1988).
18. J. A. Miller, S. J. Klippenstein, C. Raffy, *J. Phys. Chem. A* **106**, 4904–4913 (2002).
19. A. W. Jasper, J. A. Miller, *J. Phys. Chem. A* **115**, 6438–6455 (2011).
20. G. C. Schatz, G. Lendvay, *J. Chem. Phys.* **106**, 3548–3557 (1997).
21. J. Keck, G. Carrier, *J. Chem. Phys.* **43**, 2284–2298 (1965).
22. J. Troe, *J. Chem. Phys.* **66**, 4745–4757 (1977).
23. J. R. Barker, R. E. Weston Jr., *J. Phys. Chem. A* **114**, 10619–10633 (2010).
24. S. J. Jeffrey, K. E. Gates, S. C. Smith, *J. Phys. Chem.* **100**, 7090–7096 (1996).
25. S. H. Robertson, M. J. Pilling, K. E. Gates, S. C. Smith, *J. Comput. Chem.* **18**, 1004–1010 (1997).
26. P. K. Venkatesh, A. M. Dean, M. H. Cohen, R. W. Carr, *J. Chem. Phys.* **111**, 8313–8329 (1999).
27. S. J. Klippenstein, Y. Georgievskii, L. B. Harding, *Proc. Combust. Inst.* **29**, 1229–1236 (2002).
28. J. A. Miller, S. J. Klippenstein, *Phys. Chem. Chem. Phys.* **6**, 1192–1202 (2004).
29. M. Brouard, M. T. Macpherson, M. J. Pilling, *J. Phys. Chem.* **93**, 4047–4059 (1989).
30. D. G. Keil, K. P. Lynch, J. A. Cowfer, J. V. Michael, *Int. J. Chem. Kinet.* **8**, 825–857 (1976).
31. W. A. Payne, L. J. Stief, *J. Chem. Phys.* **64**, 1150–1155 (1976).
32. V. D. Knyazev, I. R. Slagle, *J. Phys. Chem.* **100**, 16899–16911 (1996).
33. N. J. Brown, J. A. Miller, *J. Chem. Phys.* **80**, 5568–5580 (1984).
34. V. Bernshtein, I. Oref, *J. Phys. Chem.* **97**, 12811–12818 (1993).

SURFACE STRUCTURE

Subsurface cation vacancy stabilization of the magnetite (001) surface

R. Bliem,[1] E. McDermott,[2] P. Ferstl,[3] M. Setvin,[1] O. Gamba,[1] J. Pavelec,[1] M. A. Schneider,[3] M. Schmid,[1] U. Diebold,[1] P. Blaha,[2] L. Hammer,[3] G. S. Parkinson[1]*

Iron oxides play an increasingly prominent role in heterogeneous catalysis, hydrogen production, spintronics, and drug delivery. The surface or material interface can be performance-limiting in these applications, so it is vital to determine accurate atomic-scale structures for iron oxides and understand why they form. Using a combination of quantitative low-energy electron diffraction, scanning tunneling microscopy, and density functional theory calculations, we show that an ordered array of subsurface iron vacancies and interstitials underlies the well-known $(\sqrt{2} \times \sqrt{2})R45°$ reconstruction of $Fe_3O_4(001)$. This hitherto unobserved stabilization mechanism occurs because the iron oxides prefer to redistribute cations in the lattice in response to oxidizing or reducing environments. Many other metal oxides also achieve stoichiometry variation in this way, so such surface structures are likely commonplace.

The properties of metal oxide surfaces are inextricably linked to their atomic-scale structure, which makes obtaining a precise structural model a vital prerequisite to understanding and modeling surface processes. The typical starting point to guess the structure of a metal oxide surface is the Tasker surface polarity criteria (1). These simple and convenient rules have proven remarkably successful for predicting the stable terminations of model systems such as TiO₂, MgO, and ZnO (2, 3). A second guiding principle to emerge from 20 years of metal oxide surface science is the vital role played by oxygen vacancies (V_Os).

The surface V_O concentration is usually in equilibrium with the bulk, where such defects form when the oxide is reduced. At the surface, V_Os strongly affect the electronic structure, are active sites for chemical reactions (4, 5), and play a central role in surface reconstructions. There exists another class of metal oxides, however, in which stoichiometric variation is accommodated primarily via the cations; the iron oxides are the prototypes. Wüstite (FeO), magnetite (Fe₃O₄), and hematite (α-Fe₂O₃) are all based on a close-packed O^{2-} anion lattice and differ primarily in the number, oxidation state, and distribution of the cations among octahedral and tetrahedral interstitial sites, Fe_{oct} and Fe_{tet} (6). Near the phase boundaries, FeO can incorporate up to 17% of Fe_{oct} vacancies, whereas the metastable phase maghemite (γ-Fe₂O₃) is essentially Fe₃O₄ with 1/6 of the Fe_{oct} removed. We now show that an ordered array of subsurface cation vacancies and interstitials underlies

[1]Institute of Applied Physics, Wiedner Hauptstrasse 8-10, Vienna University of Technology, 1040 Vienna, Austria. [2]Institute of Materials Chemistry, Getreidemarkt 9, Vienna University of Technology, 1060 Vienna, Austria. [3]Chair of Solid State Physics, University of Erlangen-Nürnberg, Staudtstrasse 7, 91058 Erlangen, Germany.
*Corresponding author. E-mail: parkinson@iap.tuwien.ac.at

the well-known ($\sqrt{2} \times \sqrt{2}$)R45° reconstruction of Fe_3O_4(001). This stabilization is driven by the material adopting a stoichiometry compatible with its environment. The oxides of Co, Mn, and Ni exhibit similar cation redistributions in reducing and oxidizing environments, so such reconstructions may be a common occurrence.

In the (001) direction, Fe_3O_4 consists of alternating planes of Fe_{tet} and $(Fe_{oct})_2O_4$ and thus appears to be a classic Tasker type 3 polar surface (1, 3). Indeed, early studies of the ($\sqrt{2} \times \sqrt{2}$)R45° reconstruction considered only structures compatible with polarity compensation (7–9). However, Fe_3O_4 is metallic, so it is not clear why the polar catastrophe should occur at all. In fact, the current model for the Fe_3O_4(001) surface is based on a nominally polar bulk truncation at the Fe_{oct}-O plane. For this termination (Fig. 1A), density functional theory–based calculations (DFT+U) (10–12) find pairs of surface Fe_{oct} relaxed in opposite directions perpendicular to the row. This structure produces the requisite ($\sqrt{2} \times \sqrt{2}$)R45° periodicity and is in qualitative agreement with undulating rows of Fe_{oct} atoms observed in scanning tunneling microscopy (STM) images (7, 8). The emergence of orbital order among the Fe_{oct} cations in subsurface layers has been likened to the "Verwey" phase of Fe_3O_4 (11), which forms below a transition temper-

ature of 125 K. This structure has been widely accepted, largely on the basis of low-energy electron diffraction (LEED IV) (12) and surface x-ray diffraction (SXRD) (10) measurements, which purport to confirm the structure. However, the quantitative measure of agreement between experimental and theoretical LEED IV curves, the Pendry R-factor (R_P) (13), was poor (R_P = 0.34) in comparison with what is achieved for metal and elemental semiconductor surfaces (R_P < 0.2). This classic study, and several others (14–16), suggest that the achievable R_P is limited for metal oxide surfaces, either because the scattering calculations fail to account for ionic bonding (14–16) or because oxides contain many defects (12).

Perspective (Fig. 1B) and top (Fig. 1C) views of the subsurface cation vacancy (SCV) structure of Fe_3O_4(001), as determined with DFT+U calculations, show that the ($\sqrt{2} \times \sqrt{2}$)R45° periodicity arises from replacing two Fe_{oct} from the third layer by an interstitial Fe_{int} with tetrahedral coordination in the second layer—a net removal of one cation per ($\sqrt{2} \times \sqrt{2}$)R45° unit cell. The subsurface reorganization distorts the surface layer, and the resulting undulations in the Fe_{oct} rows are more pronounced than in the bulk truncation model (Fig. 1, A and B). All cations in the four outermost layers possess a magnetic moment of 3.85 to 4.01 μB. This is indicative of an Fe^{3+}-like

character that is also observed in x-ray photoelectron spectroscopy (XPS) (9); angle-resolved XPS spectra are provided in fig. S1 (17). The Fe_{oct} and Fe_{tet} sublattices remain antiferromagnetically coupled as in the bulk, yielding a reduced net magnetic moment in the SCV reconstruction. The absence of Fe^{2+} suggests that the contribution of the orbital moment should be small. The magnetic moments of all atoms in the surface region are contained in table S1 (17) together with their optimized DFT+U coordinates. The energetic preference for the SCV structure is borne out by atomistic thermodynamics calculations (Fig. 1E) (18). The distorted bulk truncation is only favored below an oxygen chemical potential of –3 eV, corresponding to an O_2 partial pressure of <10^{-20} mbar at 900 K. Under such reducing conditions, however, Fe-rich surface phases occur (19). Although α-Fe_2O_3 is predicted to take over as the thermodynamically stable phase above ≈10^{-9} mbar, the ($\sqrt{2} \times \sqrt{2}$)R45° reconstruction persists up to 10^{-5} mbar. It has been shown that α-Fe_2O_3 inclusions grow slowly at 10^{-6} mbar O_2 (20), whereas conversion of the surface to γ-Fe_2O_3(001) requires extremely oxidizing conditions (9).

A key success of the SCV structure is that it explains the extraordinary thermal stability of Au, Ag, and Pd adatoms at the Fe_3O_4(001) surface, which resist agglomeration into clusters up to
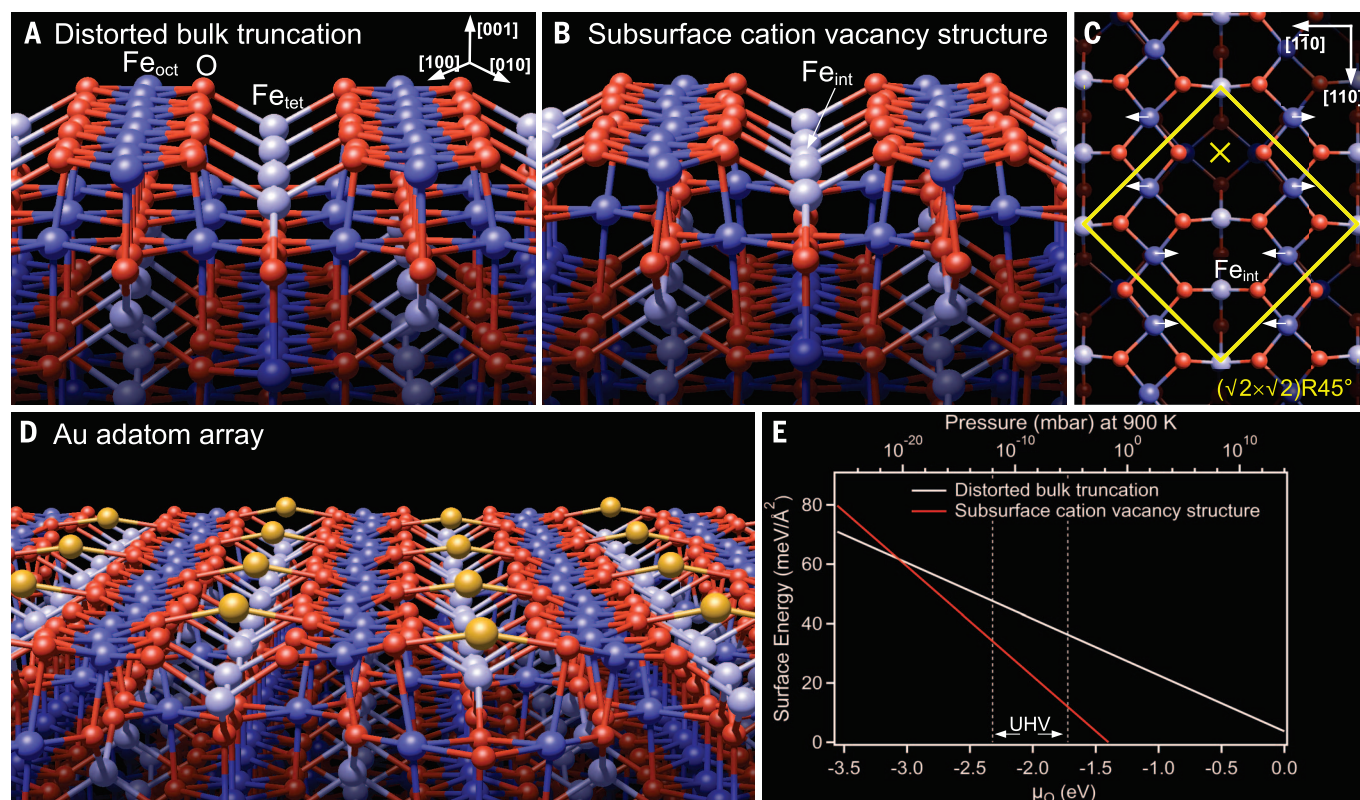

Fig. 1. DFT+U calculations show that an ordered array of cation vacancies underlies the ($\sqrt{2} \times \sqrt{2}$)R45° reconstruction of the Fe_3O_4(001) surface. (**A**) Minimum-energy structure of the distorted bulk truncation model (10, 12). (**B** and **C**) Perspective and plan views of the subsurface cation vacancy structure. A pair of Fe_{oct} cations from the third layer is replaced by an interstitial Fe_{tet} (labeled Fe_{int}) in the second layer. (**D**) Au adatoms bind strongly (2.03 eV) to surface O at positions without second-layer Fe_{tet} atoms. These sites, marked with an "×" in (C), result in a nearest-neighbor Au distance of 8.4 Å (21). (**E**) Surface energy as a function of oxygen chemical potential, μO, for both structures. The μO is converted to an O_2 pressure for a nominal annealing temperature of 900 K. The cation vacancy structure is stable in all experimentally accessible conditions.

700 K (*19, 21–23*). Adatoms exclusively occupy just one of the two available bulk continuation sites per $(\sqrt{2} \times \sqrt{2})R45°$ unit cell. This finding is difficult to reconcile with the distorted bulk truncation model because the two sites are identical save for the subtle relaxations and the subsurface orbital ordering. Unsurprisingly, DFT+U calculations for Au adatom adsorption on the bulk-truncated surface reveal no clear preference for one specific site. On the SCV structure, the interstitial Fe_{int} blocks the adsorption of an adatom in the bulk continuation site directly above. For Au, a
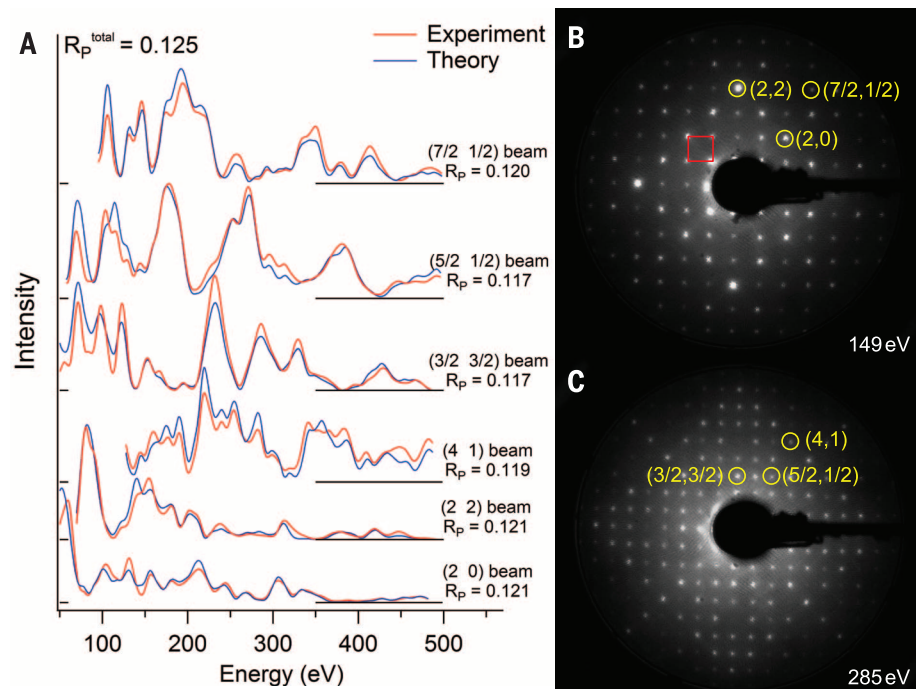
Fig. 2. Quantitative low-energy electron diffraction measurements unambiguously confirm the subsurface cation vacancy termination of $Fe_3O_4(001)$. (**A**) Comparison of selected experimental LEED *IV* spectra and theoretical curves for the optimized subsurface vacancy structure. The final R_P for the best-fit structure is 0.125; the selected beams have an individual R_P close to this average. (**B** and **C**) Experimental LEED patterns for electron energies of 149 and 285 eV, respectively. Diffraction spots highlighted with yellow circles correspond to the curves in (A). The red square indicates the $(\sqrt{2} \times \sqrt{2})R45°$ unit cell.
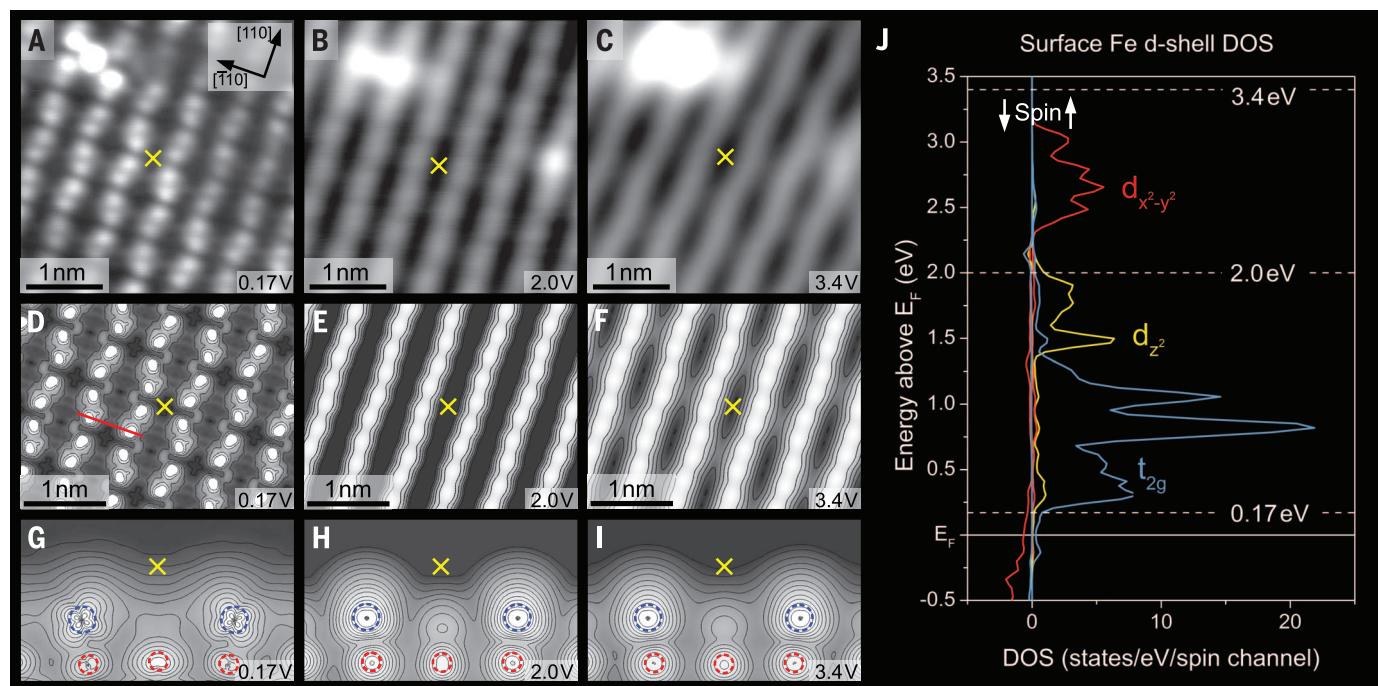

Fig. 3. STM images of the $Fe_3O_4(001)$ surface are dominated by electronic effects. (**A** to **C**) Empty-state STM images obtained on the same sample area in (A) constant-height and constant-current mode with (B) tunneling current (I_t) = 0.15 nA and (C) I_t = 0.15 nA. The bias voltages are given in each panel. An Fe adatom defect in the top left of each image defines a constant position (equivalent to the position of the yellow "×"). As the STM bias is increased, the apparent undulations in the Fe_{oct} rows reverse phase. (**D** to **F**) Simulated STM images at scanning conditions corresponding to (A) to (C).

(**G** to **I**) Electronic charge density contour plots in cross section at the position indicated by the red line in (D). The t_{2g} orbitals of the surface Fe_{oct} atoms (blue dashed circles) are distorted, resulting in a density that is asymmetric about the atom core position. (**J**) Electronic density of states above E_F for the surface Fe_{oct} atoms. As the tunneling bias is increased, different Fe d orbitals contribute to the STM images. At 0.17 V, only part of the t_{2g} orbital is accessed, followed by more spherically symmetric d_{z^2} and $d_{x^2-y^2}$ e_g orbitals at higher bias. The higher bias gives a more realistic indication of the atomic core positions.

stable binding configuration (2.03 eV) is found only in the twofold coordinated site located above the "bulk-like" subsurface region (Fig. 1D), which results in nearest neighbors 8.4 Å apart (19, 21–23).

To independently confirm the SCV structure of $Fe_3O_4(001)$, we conducted LEED IV experiments. Selected experimental spectra are shown in Fig. 2A, together with best-fit curves resulting from optimized structural parameters. [The supplementary materials contain the full set of curves (fig. S3), the optimized coordinates (table S2), their associated error estimates, and a structure file that can be opened by most visualization software programs (17).] The best-fit structure achieved $R_P = 0.125$, a vast improvement over the 0.34 obtained previously for the distorted bulk truncation model (12). Moreover, the agreement between the LEED IV parameters and the DFT+U optimized structure is excellent (table S3) (17). In the surface layer, all atoms relax toward the nearest interstitial Fe_{int} atom in the second layer (Fig. 1, B and C). The largest relaxation (0.28 Å in the surface plane) occurs for the O furthest from Fe_{int}. In DFT+U calculations, this atom has a large magnetic moment (0.35 μ_B) and is close to a –1 charge state. The lateral relaxations of the surface Fe_{oct} atoms (0.11 Å) produce a peak-to-peak undulation of 0.22 Å in the Fe_{oct} rows. Whereas the Fe_{int} atom resides 0.08 Å below the bulk-like Fe_{tet} atoms, a slight rumpling in the neighboring Fe_{oct}-O layers preserves the Fe-O bond lengths within 2% (1.889 Å).

Because STM is the method of choice for monitoring dispersed adsorbates, it is important to establish the appearance of adsorption sites in the SCV structure. Three empty-state STM images taken at the same area with different tunneling voltages are shown in Fig. 3, A to C. An Fe adatom [a typical defect after sputter/anneal cycles (24)] in the upper left corner served as a marker. Fe occupies the same adsorption site as Au, Ag, and Pd adatoms (19, 21–23), the bulk continuation site marked with the yellow "×" in Fig. 1C. At low sample bias, the undulations in the Fe_{oct} row appeared pronounced, and the × is located where the Fe rows apparently come closest together. [In our previous work (19, 21–23), we called this position the "narrow site."] When the bias was increased to 2.0 V, the Fe_{oct} rows appeared almost straight, and it was difficult to discern the $(\sqrt{2} \times \sqrt{2})R45°$ periodicity. At 3.4 V, the undulations returned, but the × was located in the opposite phase of the reconstruction, where the Fe_{oct} rows were furthest apart.

This trend was borne out in STM simulations (Fig. 3, D to F) and can be understood by examining the density of states (DOS) of the surface Fe_{oct} atoms (Fig. 3J) and the corresponding charge density contour plots (Fig. 3, G to I). At positive sample bias, electrons tunnel from the tip into empty states above the Fermi level (E_F). The d states are split by the crystal field, and the t_{2g} orbitals straddle E_F. At 0.17 V, electrons can tunnel only into a t_{2g} orbital, which is tilted off-axis because of an antibonding interaction with the underlying O-atom (Fig. 3G). Thus, the imaged electron density is not symmetric about the atom

cores. At 3.4 V, when tunneling is dominated by the symmetric d_{z^2} and $d_{x^2-y^2}$ e_g orbitals, the STM images are more in line with the true relaxations as determined with DFT+U and LEED IV.

The SCV structure described here could not have been predicted by using polarity compensation rules (3). The driving force of the reconstruction is the oxygen chemical potential, which is consistent with previous reports of reduced terminations on the $Fe_3O_4(111)$ (25, 26) and $Fe_2O_3(0001)$ (27) surfaces. Although the bulk is restricted to the FeO (rocksalt), Fe_3O_4 (spinel), and Fe_2O_3 (corundum) structures, the lack of three-dimensional periodicity at the surface permits the formation of the SCV structure, a distinct phase with an intermediate $Fe_{11}O_{16}$ stoichiometry. In this light, the $(\sqrt{2} \times \sqrt{2})R45°$ reconstruction must be seen as the first stage in the oxidation of Fe_3O_4. With all cations in a bulk-like environment, it is a highly stable configuration. It is unlikely that the structure penetrates deeper because there the interstitial Fe_{int} would prevent the occupation of a bulk Fe_{tet} site in the next layer above. The same effect is at work in the surface layer (Fig. 1D), where the Fe_{int} blocks Au adsorption in one of the bulk continuation Fe_{tet} sites.

The R_P of 0.125 achieved in our LEED IV experiments strongly supports the SCV structure and also shows that there is no inherent problem in the LEED IV methodology that limits the obtainable agreement for complex metal oxide surfaces. Although it is of course important to ensure that the surface under investigation is of the highest quality (ideally cross-checked with in situ imaging), and to minimize damage by the LEED electron beam, using the correct trial structure in the calculations is essential. To reinforce this point, we also analyzed the experimental data set acquired in a previous LEED IV study of this surface (12). Despite the crystals, vacuum system, measurement temperature, and preparation conditions differing between the measurements, a similar R_P of 0.124 was obtained.

Understanding the true structure of the $Fe_3O_4(001)$–$(\sqrt{2} \times \sqrt{2})R45°$ surface is vital to correctly interpret experimental results acquired for this surface. For example, the observation of a surface band gap was taken as evidence for a "surface Verwey transition" (11). Our results show that the modified electronic structure is in fact due to an entirely different iron oxide phase being present at the surface and is not related to charge/orbital ordering. The SCV reconstruction also likely explains why spin-polarized photoemission does not yield the 100% spin polarization predicted for the bulk (28). This surface-sensitive technique mainly probes the $Fe_{11}O_{16}$ phase, which has little DOS at E_F, no pronounced spin polarization (Fig. 3J), and a reduced net magnetization. Such a "magnetic dead layer" has been blamed for the poor performance of Fe_3O_4-based spintronics devices (29, 30). Perhaps the most exciting consequence of the SCV structure is that it supports isolated metal adatoms that remain stable against agglomeration until the reconstruction is lifted at 700 K (23, 31). This distinctive property, which represents the ultimate limit of

the adsorption template phenomenon, provides a well-defined initial state for fundamental studies of cluster nucleation and growth (22, 23) and offers an ideal model system with which to uncover the mechanisms of single-atom catalysis (32).

Given that the oxides of Co, Mn, and Ni exhibit a similar tendency to rearrange the cation lattice as the iron oxides, and even traverse the same oxidation pathway (from rocksalt structures through spinel to corundum), cation vacancy reconstructions are likely commonplace.

REFERENCES AND NOTES

1. P. W. Tasker, *J. Phys. C Solid State* **12**, 4977–4984 (1979).
2. C. Wöll, *Prog. Surf. Sci.* **82**, 55–120 (2007).
3. C. Noguera, *J. Phys. Condens. Matter* **12**, R367–R410 (2000).
4. Z. Dohnálek, I. Lyubinetsky, R. Rousseau, *Prog. Surf. Sci.* **85**, 161–205 (2010).
5. G. Pacchioni, H. Freund, *Chem. Rev.* **113**, 4035–4072 (2013).
6. R. M. Cornell, U. Schwertmann, *The Iron Oxides: Structure, Properties, Reactions, Occurrences and Uses* (Wiley-VCH, New York, 2003).
7. R. Wiesendanger et al., *Science* **255**, 583–586 (1992).
8. B. Stanka, W. Hebenstreit, U. Diebold, S. A. Chambers, *Surf. Sci.* **448**, 49–63 (2000).
9. S. A. Chambers, S. A. Joyce, *Surf. Sci.* **420**, 111–122 (1999).
10. R. Pentcheva et al., *Phys. Rev. Lett.* **94**, 126101 (2005).
11. Z. Łodziana, *Phys. Rev. Lett.* **99**, 206402 (2007).
12. R. Pentcheva et al., *Surf. Sci.* **602**, 1299–1305 (2008).
13. J. B. Pendry, *J. Phys. C Solid State Phys.* **13**, 937–944 (1980).
14. R. Lindsay et al., *Phys. Rev. Lett.* **94**, 246102 (2005).
15. V. B. Nascimento et al., *Phys. Rev. B* **75**, 035408 (2007).
16. K. Pussi et al., *Surf. Sci.* **606**, 1–6 (2012).
17. Materials and methods are available as supplementary materials on *Science* Online.
18. K. Reuter, M. Scheffler, *Phys. Rev. B* **65**, 035406 (2001).
19. Z. Novotný et al., *Phys. Rev. B* **87**, 195410 (2013).
20. S. Nie et al., *J. Am. Chem. Soc.* **135**, 10091–10098 (2013).
21. Z. Novotný et al., *Phys. Rev. Lett.* **108**, 216103 (2012).
22. G. S. Parkinson et al., *Nat. Mater.* **12**, 724–728 (2013).
23. R. Bliem et al., *ACS Nano* **8**, 7531–7537 (2014).
24. G. S. Parkinson, Z. Novotny, P. Jacobson, M. Schmid, U. Diebold, *Surf. Sci. Lett.* **605**, L42–L45 (2011).
25. N. G. Condon et al., *Phys. Rev. B* **55**, 15885–15894 (1997).
26. S. K. Shaikhutdinov, M. Ritter, X. G. Wang, H. Over, W. Weiss, *Phys. Rev. B* **60**, 11062–11069 (1999).
27. C. H. Lanier, A. N. Chiaramonti, L. D. Marks, K. R. Poeppelmeier, *Surf. Sci.* **603**, 2574–2579 (2009).
28. J. G. Tobin et al., *J. Phys. Condens. Matter* **19**, 315218 (2007).
29. W. Kim, K. Kawaguchi, N. Koshizaki, M. Sohma, T. Matsumoto, *J. Appl. Phys.* **93**, 8032 (2003).
30. X. W. Li, A. Gupta, G. Xiao, W. Qian, V. P. Dravid, *Appl. Phys. Lett.* **73**, 3282 (1998).
31. N. C. Bartelt et al., *Phys. Rev. B* **88**, 235436 (2013).
32. X.-F. Yang et al., *Acc. Chem. Res.* **46**, 1740–1748 (2013).

SUPPLEMENTARY MATERIALS

Science

AAAS

Subsurface cation vacancy stabilization of the magnetite (001) surface

R. Bliem *et al.*
Science **346**, 1215 (2014);
DOI: 10.1126/science.1260556